Received: 15 December 2018 | Revised: 8 April 2019 | Accepted: 23 April 2019

DOI: 10.1002/ctpp.201800180

ORIGINAL ARTICLE

Contributions to Plasma Physics

Condensation of laser-produced gold plasma during expansion and cooling in a water environment

Yu.V. Petrov[1,2] | N.A. Inogamov[1,3,4] | V.V. Zhakhovsky[3,4] | V.A. Khokhlov[1]

[1]Landau Institute for Theoretical Physics of the Russian Academy of Sciences, Chernogolovka, Moscow Region, Russia

[2]Moscow Institute of Physics and Technology, Dolgoprudny, Moscow Region, Russia

[3]Joint Institute for High Temperatures of the Russian Academy of Sciences, Moscow, Russia

[4]Dukhov Research Institute of Automatics, Moscow, Russia

Correspondence
N.A. Inogamov, Landau Institute for Theoretical Physics of the Russian Academy of Sciences, 1-A Akademika Semenova Avenue, Chernogolovka, Moscow Region 142432, Russia. Email: nailinogamov@gmail.com

Physical processes involved in laser ablation in liquid (LAL) are studied using a gold target irradiated through transparent water. During and after irradiation, the heated material from the surface of a target produces a plume that expands into liquid-forming nanoparticles (NPs). The LAL method of NP production is ecologically much cleaner than others. A better understanding of the processes associated with complicated hydrodynamic phenomena leading to LAL is important for controlled manufacturing. We consider laser pulses with different durations τ_L covering fifth orders of magnitudes ranging from 0.1 ps to 0.5 ns and large absorbed fluences F_{abs} near optical breakdown of liquid. It is shown that the trajectory of the contact boundary with liquid at the middle and late stages after passing the maximum intensity of the longest pulse is rather similar for very different pulse durations if energies F_{abs} are comparable. We trace how hot (in a few eV range) dense gold plasma expands, cools down, intersects a saturation curve, and condenses into NPs appearing first inside the water-gold diffusively mixed intermediate layer where gold vapour has the lowest temperature. Later, the pressure around the gold-water contact drops down below the critical pressure for water. As a result, the nanoparticles find themselves in gaseous water bubble where density of water gradually decreases to $10^{-4} - 10^{-5}$ g/cm^3 at maximum bubble expansion.

KEYWORDS
laser ablation in liquid, laser gold plasma, nanoparticles

1 | INTRODUCTION

Importance of wide variety of nanoparticles (NPs) produced by laser ablation in liquids (LAL) and the corresponding technological aspects were recently reviewed extensively.[1,2]

As usual, engineering challenge coming from the real life brings a lot of physical problems belonging to separate fields. The present work on NP/LAL is significant in the fundamental sense because it links together these scientific fields including propagation of shock waves in condensed media, first order equilibrium, and non-equilibrium phase transitions (melting/solidification, evaporation/condensation) in moving gold and water, and atomic solvability of gold in water. For the last, it is necessary to know transport coefficients, e.g., diffusion coefficients defining intermixing between contacting materials. We consider transformation of dense hot plasma states of gold into a rather low-temperature two-phase vapour–liquid mixture with growing NPs. The transformation takes place in the surrounding liquid. Both gold and water transit from the overcritical densities to subcritical ones during heating, expansion, and cooling processes. The passage through the near-critical densities causes a strong increase in compressibility. Gold transits to the soft states first, water also follows this way later. There are three ranges relative to the degree how rigid/soft material is. The factor $\gamma = d(\log(p))/d(\log(\rho))$ is high (e.g, ~3 and more) in condensed

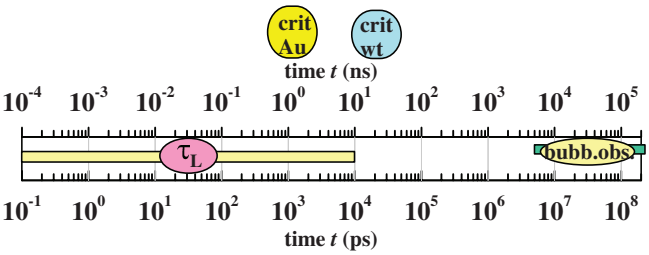

FIGURE 1 The hierarchy of time scales for the consequence of processes in gold target under water triggered by laser pulse. Durations of pulses τ_L usually used in LAL are from ~0.1 ps to ~10 ns. High-speed camera records appearance, expansion, and collapse of a bubble over the range marked as "bubb. obs.", as it was reported in ref. [3]. We see that such observations are difficult in the stages preceding the bubble formation. Pressure $p_{CB}(t)$ near the Au-water contact boundary (CB) decreases with time. First it drops below critical pressure for gold and after that—below critical pressure for water. Corresponding stages are marked as "crit Au" and "crit wt"

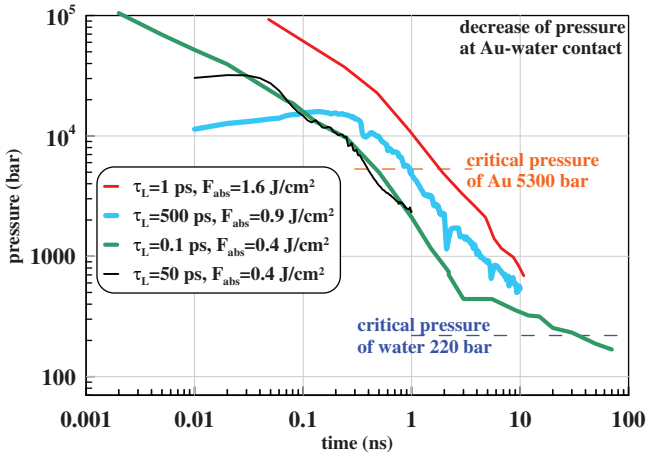

FIGURE 2 Pressure at a gold-water contact. The upper curve (the red curve) is taken from molecular dynamics (MD) simulation, which will be described in this article below. Other three dependencies are results of hydrodynamic simulations. Unloading of shock-compressed water decreases the contact pressure $p_{CB}(t)$. Thus, it drops first below the critical pressure for gold and after that below the critical pressure of water. These stages are marked in Figure 1 as "crit Au" and "crit wt." The evolutions corresponding to the pulse with $F_{abs} = 0.4\,J/cm^2$ and $\tau_L = 0.1$ ps are taken from the work[4]

states, but in gaseous states above the critical point a thermal contribution to pressure becomes significant and γ reaches ~1.4 to 2, while in two-phase liquid–vapour mixture, it has the lowest values nearby $\gamma \approx 1 + \varepsilon$, $\varepsilon \ll 1$.

Formation of a bubble is a consequence of softening of water. Evolution times of typical LAL cover a very wide range of times shown in Figure 1. For femtosecond laser exposure, this range consists of ninth orders of magnitudes starting from the pulse duration τ_L and ending at the time when the bubble achieves its first expansion maximum. And only last two orders can be recorded by ultrafast camera, see the recent detailed studies in ref. [3]. It is convenient to describe the initial stages in picoseconds for femtosecond and picosecond exposure times. Middle stage is measured in nanoseconds, while a semi-spherical bubble is formed and begins to expand during the final stages lasting microseconds. These ps-ns-μs stages are illustrated in Figure 1.

Pressure at a contact boundary (CB) $p_{CB}(t)$ plays an important role. During heating by a laser pulse, this pressure increases to its maximum at the pulse end. Then, it decreases gradually with time after the pulse as it is shown in Figure 2 where the plotted simulation data are partially taken from the work.[4] This is definitely seen for the pulses with durations τ_L equal to 50 and 500 ps. It is important that the descending part of the function p_{CB} below ~1 GPa is universal relative to the pulse duration. The function $p_{CB}(t)$ is approximately described as a decreasing power function of time with a coefficient proportional to energy absorbed during a laser pulse:

$$P_{CB}(t) = 5 \times 10^3 F_{Jcm2}/t_{ns}^{1.05}[\text{bar}] = 0.5 F_{Jcm2}/t_{ns}^{1.05}[\text{GPa}], \quad (1)$$

where $F_{Jcm2} = F_{abs}/1$ [J/cm^2] is the absorbed energy, $t_{ns} = t/1$[ns] is the time in nanoseconds reckoned from a maximum of the Gaussian pulse $I = I_0 \exp(-t^2/\tau_L^2)$.

There are five expansion stages. The first stage corresponds to heating of a target by a laser pulse. It is well seen in Figure 2 for pulse durations τ_L equal to 50 and 500 ps. For ultrashort pulses, the pressures at the first stage are high, thus they are not shown in Figure 2; for the shot with $F_{abs} = 0.4\,J/cm^2$ and $\tau_L = 0.1$ ps (the green curve in Figure 2), the first stage is presented in detail in [4].

The second stage is transient with a decay rate of the contact pressure slower than $\propto 1/t$. The last decay rate defines the third stage, see Equation (1). The second stage almost disappears for a nanosecond pulse shown by the blue curve in Figure 2. However, it is clearly presented for shorter pulses, even for the pulse with $\tau_L = 50$ ps. This is because there are nucleation, rupture, and foam formation after the short pulses lasting tens of picosecond, until $\tau_L = 50$ ps. Internal layers of foam move faster than the "atmosphere" created by the deceleration of the contact by water. Resistance of the water to expansion of a gold plume is discussed in ref. [4] providing explanations of this phenomenon. The inflow of foam into a contact plug or "atmosphere" was observed also in ref. [5–7] where the ultrashort pulses at moderate energies F_{abs} were considered. Thus, the ram pressure

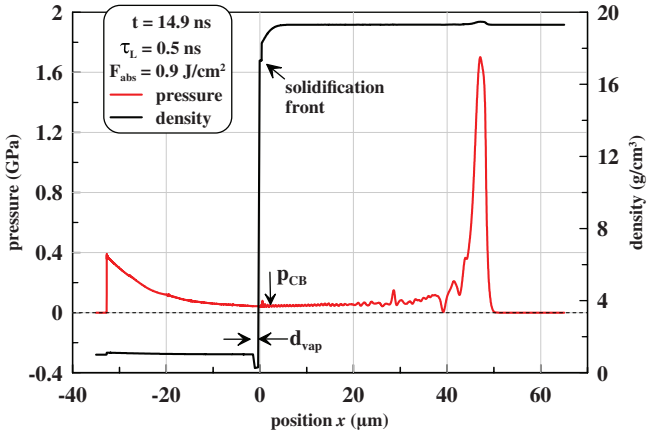

FIGURE 3 Pressure and density profiles near the contact layer between two shocks. p_{CB} is a contact pressure plotted as a blue curve in Figure 2. Position x is the distance from an initial position of Au-water contact boundary (CB). The arrows d_{vap} mark the current boundaries of a gaseous gold (vapour) layer. The left arrow d_{vap} points at CB while the right arrow d_{vap} points at a boundary between gaseous and liquid gold

of foam "accreting" (see ref. [4]) onto the atmosphere impedes the deceleration of contact by water resistance. Appearance of the ram pressure is a result of the inflow of momentum into the atmosphere. This inflow compensates partially the deceleration and the decay of contact pressure.

Therefore, thanks to this compensation the contact pressure decreases more slowly at the second stage than in the third stage. At the third stage, the ram support from the foam ends and the deceleration rate of contact by liquid increases. For nanosecond pulses, this support does not exist as shown by the blue curve in Figure 2. There, the nucleation and formation of foam are not seen because the heating time is much longer than the acoustic time $t_s = d_T/c_s \sim 30$ ps, where d_T is the thickness of the heated zone or the ablated layer, $c_s \approx 3$ km/s is the speed of sound in gold.

Very thick foamy layer is formed by an ultrashort pulse with large absorbed energy F_{abs}. The foam inflates greatly (for expansion into vacuum) and becomes many times thicker than the thickness of the heated zone or the ablated layer, thus the volume fraction of liquid in the foam becomes small. The inflation process lasts longer and longer time as fluence F_{abs} increases, up to hundreds of nanoseconds, see ref. [8].

At the third (III) stage (1), the contact pressure is determined by the pressure of approximately adiabatic gaseous gold in one-phase states above the condensation curve and by room released by retreating water (the pressure drop is a result of expansion of a layer filled by gaseous Au). The fourth stage (IV) of evolution is characterized by formation of two-phase states of gold. It happens when expanding gold intersects the condensation (or saturation, or equilibrium) curve and begins to form the clusters of a few atoms, which are growing into NPs (hundreds and more atoms together). At the fourth stage, the compressibility of gold achieves its maximum. It is larger than that at the third stage where gold was in one-phase states; let us mention that compressibility of one-phase gaseous gold is larger than compressibility of dense gold with densities higher than the critical density $\rho_{crit} \approx 5.3$ g/cm^3 of gold.

At the fourth stage, the pressure $p(\rho, s)$ of gold becomes softer (an adiabatic factor drops to $\gamma \approx 1$), therefore, the decrease of contact pressure with time as gold expands becomes more slower relative to the rather fast decay $p_{CB} \propto 1/t$, see (1) and Figure 2; here s is entropy. The kink in the contact pressure $p_{CB}(t)$ is due to transition through the condensation curve, which is seen on the green curve shown in Figure 2. Obviously, the kink marking the change of stages III and IV should be below the critical pressure of gold. The position of the kink depends on temperature (it is better to say on entropy s) of gaseous gold—the higher s the larger the expansion and longer time is required for the III → IV transition. At the fourth stage, the pressure of high-entropy gold equals to the saturated vapour pressure $p_{sat}(T)$ at a given temperature. This means that the intensive formation of NPs begins due to the condensation process. The fifth stage begins when the contact pressure begins to be determined by the pressure of gaseous water, see next Sections.

Figures 3 and 4 show propagation of shocks in water and in gold. We see how far those shocks are separated relatively to very thin layers of vapourized and molten gold $d_{vap} \sim 1$ μm. Still the one-dimensional approach is valid because a path passed by a water shock is much less than radius R_L of a laser beam. We will take into account the value $R_L \approx 250$ μm given in ref. [3] where it was determined by a crater diameter. The shock in gold is insignificant for dynamics of vapourized gold and water.

Finite pressure p_{CB} in the intermediate region between shocks (see Figure 3) is formed due to water resistance to ablative expansion of hot gold. For expansion in a vacuum, the pressure at the bottom of the future crater is zero at the rather late stage shown in Figures 3 and 4. Let us mark also that the vapourized gold is mainly expanding at the stage shown in those figures as seen from velocity gradients near the boundary of condensed gold. The last fact will be discussed with more details below. Large volume expansion of thin high-entropy gold and water layers (as pressure decreases) will be opposed to small volume expansion of surrounding the condensed gold and cold water.

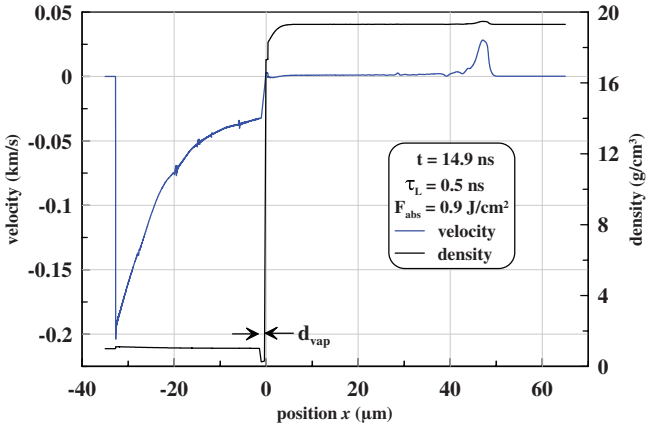

FIGURE 4 Velocity and density profiles. Position x is the distance from an initial position of Au-water contact. We see that condensed gold (liquid and solid, see the arrow "solidification front" in previous Figure 3) is motionless except the layer occupied by a shock wave moving through the bulk gold to the right side. Thus the right boundary of the vapourized gold layer d_{vap} is at rest

2 | METHODS

We use two approaches to understand physics of ablation in liquid. The first of them is the hydrodynamic approach based on a finite-difference Lagrangian one-dimensional scheme. Molecular dynamics (MD) is employed as the second approach. These two approaches complement each other. Thus, we get an extended and reliable description of what is happening in an Au-water system.

2.1 | Hydrodynamic code

Our finite-difference Lagrangian one-dimensional scheme includes two energy equations: electron and ion subsystems are treated as the connected through electron-ion coupling but thermodynamically independent subsystems. Corresponding system of equations smoothly transits from two-temperature states to usual one-temperature states as electron and ion temperatures tend to each other at all points occupied by the substance. Thus, we can equably study the two-temperature and one-temperature situations without applying different schemes for each of them. The system and the approach were described in detail in our previous works.[4,9] The details include: conservation laws, equations, initial and boundary conditions, energy absorption, equations of state for metal and for liquid, thermal conduction, and electron-ion coupling.

The basic scheme of numerical solution is taken from ref. [10], where it was developed for the one-temperature conditions. We added the second energy balance and split the energy equation into two equations: one for electrons and second for ions. According to ref. [10], the system of equations is solved by an implicit finite-difference method. We separate the thermal conduction and hydrodynamic cycles of iterations inside one time step. Artificial viscosity is employed to suppress oscillations. The hydrodynamic iterations are executed in accordance with the conservative scheme described in ref. [10].

The balance equation for electron energy is solved taking the density and velocity profiles from the hydrodynamic iterations. Electron-ion energy exchange is calculated in every Lagrangian cell taking profiles of electron and ion temperatures from previous iteration. The procedure retains conservation character of the scheme. Using densities from the hydrodynamic stage and temperatures (electron and ion) from the thermodynamic stage, the electron and ion pressures are calculated.

A sum of those partial pressures is a total pressure. A profile of total pressures along the chain of Lagrangian cells is used in the hydrodynamic stage of the next iteration. Convergence of iterations is controlled. Such control defines a time step—if convergence is fast, then the time step is enlarged.

For an ion subsystem, we use tables of a wide-range equation of state.[11–15] Thermodynamic electron additions, coefficients of thermal conduction, and electron-ion coupling parameter are taken from ref. [16–18]. This hydrodynamic approach was used in our previous articles devoted to physics of laser ablation.[4,19]

2.2 | MD code

Below, we use the MD approach similar to the approach used in ref. [4]. The initial length of a water-gold system was 4 μm. The initial position of a CB between gold and water was at $x = 0$. The total length of the narrow MD box along the axis x is 8 μm. The cross section of 10 nm × 10 nm × 10 nm is small because it is required for following the long-time evolution of a system.

The initial number of atoms of gold was 11,279,232. To speed up MD simulations, we cut the deep layers of gold after cavitation and formation of foam. A total of 1,780,214 atoms of gold remains after cutting. The same procedure was used in ref. [4]. It has no effect on evolution of the layers near the contact.

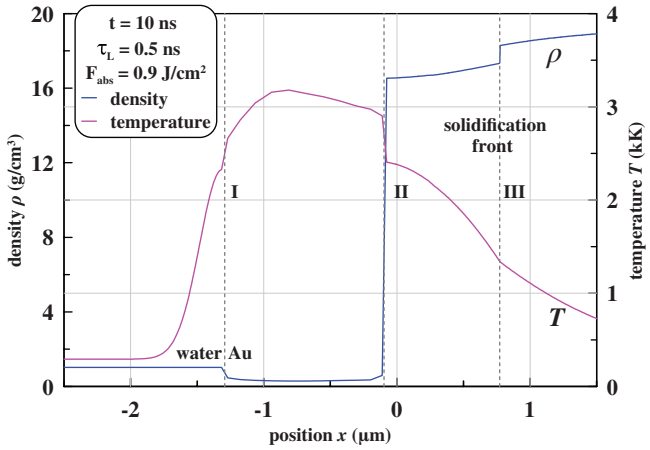

FIGURE 5 Structure of a contact layer according to approximations used in our hydrocode discussed in the text. The layer consists from gaseous gold (located between I and II) and a zone of hot water near the contact boundary marked as I. Our hydrocode is based on splitting of mass along the spatial axis into a Lagrangian mesh. The code does not include mutual diffusion of gold atoms and water molecules. Therefore the contact boundary I remains sharp. The number III marks solidification front associated with freezing, which is discussed in the text

Initially, there are 6,372,951 particles of water. We use the same method of cutting of a part of a water layer as it is described in detail in ref. [4]. After this cutting, the water layer is located between a contact and a moving piston. Trajectory of the piston was defined in the preliminary simulations, see ref. [4]. There are 1,597,495 particles in water after activation of the piston.

EAM potential for gold was developed in ref. [20] For water, the potential described in www.researchgate.net/project/Development-of-interatomic-EAM-potentials was employed.

3 | STRUCTURE OF HIGH-ENTROPY LAYER ACCORDING TO HYDRODYNAMIC SIMULATIONS

In Figures 3 and 4, an integral picture at a rather late instant of time is shown. It includes the whole Au-water layer between two shocks. The thin layer around d_{vap} in Figures 3 and 4 is the most interesting place for technologies of NPs production.

Figure 5 presents the structure of a contact layer d_{vap} obtained by using a hydrodynamic code. This code was described in ref. [4]. Modification introduced into the code in the present article relates to thermal conductivity of water. Thermal conduction in water was neglected in ref. [4]. A layer of hot water appears thanks to conduction, see Figure 5. Of course, water conduction is weak in comparison with condensed gold, but it is important because we want to understand how a bubble is formed and how gold NPs and atomic gold are mixed with gaseous water inside a bubble.

Indeed, there are two sources of heating of water. The first one is connected with dissipation in shock (entropy trace after shock). As we will see below, this source is weaker than the conductive source (the second source of heating); dissipation power non-linearly depends on the Mach number of shock; for long pulses, the dissipation is negligibly small. Thus, conduction is important. However, the first source (in the cases with short pulses) creates a wider layer of heated water than the second source, see MD simulations below.

In the particular simulation presented in Figures 3–5, the coefficient κ of thermal conduction of water was taken equal $\kappa_{\mathrm{eff}} = 6$ $\mathrm{W^{-1}\ m^{-1}\ K^{-1}}$; $\kappa = 318\ \mathrm{W^{-1}\ m^{-1}\ K^{-1}}$ for gold under normal conditions; κ for gold in a wide range of temperatures and densities is taken from refs. [16,17,21]. Thickness of a heated water layer is $d_{\mathrm{wt}}(t = 10\,[\mathrm{ns}]) = 0.22$ μm (FWHM) at the instant $t = 10$ ns shown in Figure 5. History of heating of water from gold and propagation of heat in water is complicated because thermal conductivities κ of gold and water significantly change thanks to wide variations in temperature and density. The coefficient κ of gold in gaseous states in the layer between boundaries I and II in Figure 5 is very small. Thus, heat absorbed by water is accumulated during rather early stages (before the instants shown in Figures 3–5), when gold near a contact was dense and better conducting.

In this article, to describe heating of water, we use effective coefficient $\kappa_{eff} = 6$ W/m/K. Coefficient κ_{eff} is 0.3–0.75 $\mathrm{W^{-1}\ m^{-1}\ K^{-1}}$ in *liquid* water in a pressure range 1–1,000 bars, see ref. [22]; transport in liquid and gaseous water is very different. Thermal diffusivity $\chi = \kappa/C$ is used when solving the heat conduction equation $T_{\mathrm{t}} = \chi T_{xx}$, here C is the heat capacity per unit of volume. Thermal diffusivity χ is ~0.001 $\mathrm{cm^2/s}$ for liquid water. Coefficient χ for gaseous overcritical water is roughly $\chi \sim 0.03\ \mathrm{cm^2/s}$ for $p = 100$ bar, $T = 1.2$ kK.[22] This coefficient is 30 times larger than the coefficient for liquid water. However, heat capacity per molecule is decreased from $\approx 9k_{\mathrm{B}}$ in liquid to $\approx 3k_{\mathrm{B}}$ in gas. Therefore, we use as an approximate effective thermal conductivity for water the value $\kappa_{\mathrm{eff}} = 6\ W^{-1}\ \mathrm{m^{-1}\ K^{-1}}$. Additional information following from MD simulations is given below.

Redistribution of heat due to conduction before the geometrical transition of a plane (disk type) layer of hot water in a bubble with semi-spherical shape continues up to a few microseconds.[3] Thickness of the layer with high entropy water before

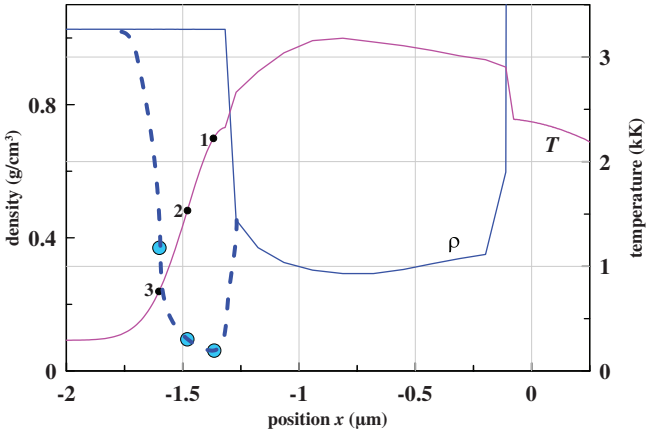

FIGURE 6 This is an enlarged view of the contact layers taken from the previous Figure 5. The layer of hot water is adjacent to the gaseous gold layer. Uncorrected density profile is shown by the solid blue curve. Correction of density shown by dashed curve results from the thermal expansion of water at given pressure due to the rise of temperature. The corrected density is smaller inside the hot water layer. Three blue circles are described in the text

transition to a semi-spherical bubble is

$$d \sim d_{\mathrm{wt}}(t = 10\,[\mathrm{ns}])\sqrt{t_{\mathrm{geom}}/(t = 10\,[\mathrm{ns}])} \sim 2 - 5\,[\mu m], \tag{2}$$

where t_{geom} is 1–5 μs. The layer (2) is very thin in comparison with typical diameters of a laser beam ~500 μm. Hydrodynamic expansion velocities overcome velocities of heat conduction spread $v_T \sim \sqrt{\chi/t}$ ($V_{\mathrm{T}} \sim 1$ m/s for $\chi = 0.03$ cm^2/s and $t = 1$ μs) during and after transition.

Hydrocode used employs a simplified version of the equation of state for water. It is taken from a Hugoniot (or shock) adiabatic curve, see refs. [4,23,24]. This is an one-argument function giving dependence of pressure in water as a function of water density: $p_{\mathrm{Hug}}(\rho)$, see (12) in ref. [4]. Temperature field calculated in water by the hydrocode does not influence the dependence $p_{\mathrm{Hug}}(\rho)$ and thus the density profiles $\rho(x, t)$ in water. Therefore, density of water is approximately 1 g/cm^3 near the contact I in Figure 5 and in Figure 6 (the blue continuous curve); the adiabatic curve $p_{\mathrm{Hug}}(\rho)$ (12) in ref. [4] returns to uncompressed water in normal conditions when pressure drops down significantly below bulk modulus 1.5 GPa for water. This is the reason why the blue continuous curve presenting density profile in Figures 5 and 6 has density ≈1 g/cm^3 in water close to the contact I.

Correction to density of water due to its heating is given in Figure 6 by the dashed blue interval. Let us say how we have calculated this correction. First, take pressure $p = 600$ bar in the contact region for the instant $t = 10$ ns shown in Figure 6; see Figures 2 and 3 where pressures are present. We suppose that this pressure moderately depends on the correction. Second, choose three points 1, 2, and 3 at the temperature profile of hot water in Figure 6. Take temperatures T_j, $j = 1$, 2, and 3 in these points. Third, use the equation of state for water $p(\rho, T)$ to calculate densities ρ_j for these pairs (T_j, p) from equations $p(\rho_j, T_j) = 600$ bar. We use the equation of state for water given in ref. [25].

We plot values of obtained densities ρ_j at the same positions x_j where the points 1, 2, and 3 in Figure 6 are placed. Thus, the blue-dashed interval going through the three blue circles x_j, ρ_j in Figure 6 appears. We see that water in the hot layer also (as gold) very significantly expands even at rather significant load—600 bar. At the instant $t = 10$ ns, the pressure in water 600 bar becomes larger than critical pressure 220 bar for water. In the dashed interval, the water is in the gaseous overcritical state. Below, we will return to consideration of decrease of pressure to low values much smaller than 220 bar. This will be prolongation of the dependencies in Figure 2 down to 0.1–1 bar.

Thermal conductivity in condensed gold remains high. Thus, the layer of molten gold seen in Figures 3–5 will be solidified in next few tens of ns: $\sim d^2_{\mathrm{molten}}/\chi_{\mathrm{Au}}$. Surface structures are formed during solidification. Vapour plume in the case of long (ns) pulses weakly affects these structures during solidification.

4 | STRUCTURE OF HIGH-ENTROPY LAYER ACCORDING TO MD

The effective approach to solve problems related to LALs is based on the MD approach.[4–7,23,24,26,27] Hydrodynamic simulations presented above and MD compliment each other. Figures 7 and 8 illustrate the MD results. In Figure 7, the HD and MD density profiles are compared. The HD code does not include diffusion. Thus, the HD contact is atomically sharp. From Figure 8, it is obvious that diffusion is important for NPs formation. We have strong intermixing of gaseous gold and gaseous water in the case simulated by MD and shown in Figures 7 and 8. There is the second drawback in the HD-code; the first is the absence of diffusion. It relates to the description of thermodynamics of gaseous gold. We use a sum of electron and ion free energies $F_{\mathrm{e}} + F_{\mathrm{i}}$ to obtain pressure. The particular expression for electron pressure $p_e > 0$ has inaccuracy $\sim 0.01 - 0.1$ GPa. This inaccuracy is

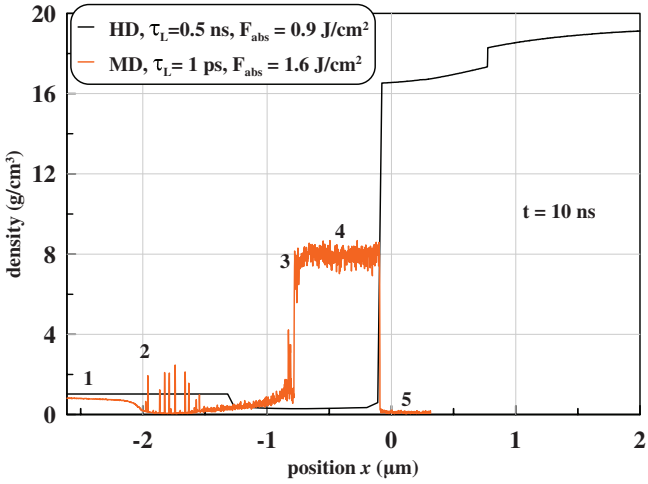

FIGURE 7 Water heated by a shock passed through water some time ago is denoted as "1". "2" is the left edge of the diffusion layer located between 2 and 3. The needles near the 2 and 3 are the gold clusters. Thus condensation develops heterogeneously starting from the edges. Formation of the clot 4 and the rarefied region 5 is discussed in text

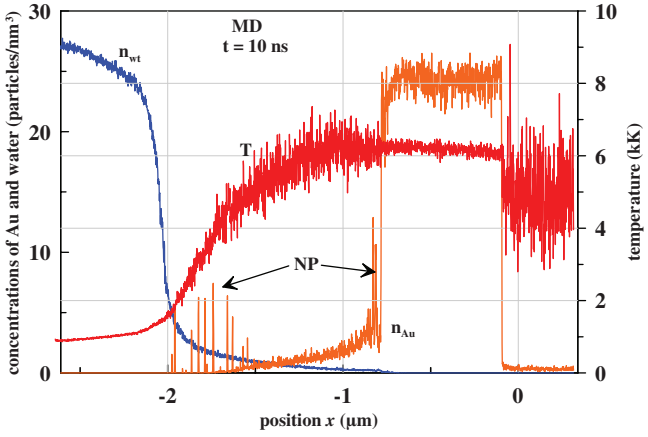

FIGURE 8 Previous Figure gives the total density of water-gold mixture in the mixture region. Here, we separate concentrations of gold $n_{Au}(x, t)$ and water $n_{wt}(x, t)$ for $t = 10$ ns. Thus the diffusion layer and water-Au interpenetration becomes clear. The temperature profile "T" shows definite decrease into the water side. Thus it seems that diffusion overruns heat conduction to some extent. The two forests of the needles marked by the arrows "NP" (nanoparticles) present condensation process creating NPs

insignificant when pressures are at the GPA level. However, due to this inaccuracy, we overestimate total pressure $p = p_e + p_i$ of gaseous gold in the states with temperatures below ≈5 kK. Additional simulations will be made in future with exclusion of this drawback. Then, density of gaseous gold should be higher and the thickness of the layer occupied by the gaseous gold should be more narrow. Comparison of the HD and MD simulations in Figure 7 says that nevertheless the real situation is approximately well described down to pressures $\sim 10^3$ bar. Estimates relating to the evolution at the much lower pressures are given in the next section.

Diffusion and heat conduction operate approximately at the same rate. This conclusion follows from Figure 8. We see only the narrow layer of pure hot water ahead of the diffusion layer, this is the layer to the left from the digit "2" in Figure 7, where density of water is decreased. (The layer of hot pure water is narrow relative to thickness of a diffusion layer.) In Figure 8, this layer locates between the region of steep decrease of concentration of water molecules $n_{wt}(x, t)$ and the first needle from the forest of needles at the left side of a diffusion layer. Let us mention that water at some distance from the diffusion layer (region 1 in Figure 7) is heated to temperatures near 1 kK, see Figure 8. This heating is the dissipative trace of strong shock compression at the early stage in the case with an ultrashort pulse.

Why diffusion is important for condensation? The pressure profile is approximately homogeneous along the layer of liquid water (region 1 in Figure 7) and in the diffusion layer; the last is filled with a mixture of gaseous water and gaseous gold. Above, we judge about the question is matter in the one-phase gaseous state or in the two-phase vapour–liquid state comparing pressure p and vapour saturation pressure $p_{sat}(T)$ at given temperature: condensation begins if $p < p_{sat}(T)$. However, this conclusion is valid for pure matter. In the case of mixture, when we decide gaseous gold will condense or not, we have to compare not total pressure of mixture p_{total} with p_{sat} but partial pressure of gaseous gold p_{Au} dissolved in water with p_{sat}; $p_{total} = p_{Au} + p_{wt}$.

In the case shown in Figure 8, we have diluted solution of atomic gold at the left edge of the diffusion layer. Total pressure 1,000 bar is rather high (it is above saturation pressure for this temperature—therefore, condensation is delayed in the middle of the diffusion layer) in MD simulation at the instant $t = 10$ ns shown in Figures 7 and 8. However, at the left edge of the diffusion layer, partial pressure p_{Au} is below $p_{sat.}$ Also water particles act as a buffer gas, which serve for withdrawal of latent heat of condensation in a pair Au-Au collisions thus enhancing the rate of condensation. Therefore, the formation of NPs begins and

continues at the left edge. The condensed NPs manifest themselves as the sharp needles at the density and gold concentration profiles in Figures 7 and 8. They are marked by the left arrow in Figure 8 going from the note "NP" (nanoparticles).

The second group of NPs (group of the needles) appears and begins to grow at the right edge of the diffusion layer. At this edge, temperature is slightly lower while density of gaseous gold is a few times higher than in the middle. Let us consider this situation (we compare the middle and the right edge) at the density-pressure phase diagram. Let us imagine the condensation curve $\rho_{sat}(p)$ at this plane ρ, p. Then, the middle is outside the condensation curve $\rho_{middl} < \rho_{sat}(p)$ while the right edge of the diffusion layer is inside $\rho_{right} > \rho_{sat}(p)$ because density is higher, here p is the pressure across the diffusion layer at the instant shown. Thus, condensation and NPs (needles) appear at the right edge—this place is marked by the right arrow going from the note" NP" in Figure 8.

The hydrodynamic (HD) code used is described in our previous articles.[4,23,24,27] In this article, as was said above we add conductivity of water to the HD code. Density profile obtained from the HD code is given in Figures 5–7. The HD simulated case relates to the long (nanosecond) pulse. It is important that in this case we do not see nucleation, formation of foam, breaking of foam, and separation of the right side of the gaseous-foamy layer from the bottom of the future crater; we say here "the right side" because laser beam comes from the left side as shown in our figures.

The MD simulation relates to the ultrashort laser pulse. In this case, we have foaming, breaking, and separation of foam. Descriptions of these stages need a separate text. Here in Figures 7 and 8, we show the rather late stage achieved during our simulation. Formulation of problem solved by the MD code is as follows. We have a long computational cell with 2 μm of water and 2 μm of gold and 10 nm × 10 nm ×10 nm cross section, see also descriptions in [4,23,24,27]. We did preliminary simulations defining the trajectory of water particles $x_{400}(t)$ located before a laser pulse rather outside (400 nm outside) to the initial position of the water-gold contact. The trajectory is defined along a range of times up to the instant when a rarefaction wave reflected from the free surface of water (free surface is placed initially at the distance −2 μm from initial contact) comes to our marked water particle x_{400}. After that, we use this trajectory and its analytical continuation in time as the left boundary of the computational cell to decrease the number of atoms in simulation.

We follow evolution of a thick gold target up to the stage when the foam separates from the bottom of a crater. This takes place at a depth of ≈450 nm below (to the right side) from the initial position of a contact—the point $x = 0$ in our figures—for the MD shot presented here. After that, we delete atoms of gold to the right from this bottom because, indeed, the approximately motionless condensed part of a rest of a gold target plays an insignificant role in the evolution of a separated plume. We put the right boundary condition at this depth. The condition deletes gold atoms, which achieves this depth. Then, gradual formation of the clot 4 and the rarefied region 5 in Figures 7 and 8 takes place.

Evaporated/ablated mass of gold in HD simulation of a nanosecond action is ≈20 nm at an initial density of 19.3 g/cm^3. While in the case of the ultrashort action with larger energy F_{abs}, this mass is ≈400–500 nm; see Figures 7 and 8 where the point $x = 0$ corresponds to the initial position of a contact in both the HD and MD cases. Cooling and recrystallization in the condensed residuals of the gold targets in the both cases proceeds faster than evolution of the plume. Therefore, the plume evolutions are very different in the cases with ablation in a vacuum or gas versus ablation in liquid—this was emphasized in several articles.[4–7,23,24,27] While the solidification process and thus formation of surface structures are much less depending on the environment (vacuum or liquid), e.g., the random surface structures (RSS) produced by ultrashort pulse are the same in the cases with ablation in a vacuum and in liquid. This conclusion follows from analysis of dynamics of the plumes given above.

Appearance of the RSS after ultrafast single-shot action was demonstrated in articles by Vorobyev and Guo.[28,29] First explanations connecting the RSS and foaming/rupture of foam and fast (before their disappearance thanks to surface tension) freezing of the cellular capillary remnants of foam (the remnants are: membranes, jets, and droplets) were given in ref. [30,31] later confirmed in ref. [32–36]. These results relate to the RSS observed after the single-shot ablation into vacuum. According to conclusion given in the previous paragraph, the same RSS structures should be formed if ablation in liquid is initiated by an ultrashort pulse. Indeed, the previous observations (see Figure 8 in refs. [37,38]) and recent direct comparisons of RSS in gas and in liquid (see Figure 2 in refs. [39,40]) confirm the conclusion. It is worth noting that the weakly pronounced structures are formed after the nanosecond pulses.

5 | LATE STAGES, LOW PRESSURES

At the present stage of studies, we do not have longer simulations than shown above. Future work will be continued using the transport coefficients for hot rarefied matter like those given in refs. [41,42]. It is plausible that the conductive cooling is slow at the late stages. Then, it is worth following the adiabatic expansion till very low pressures. Let us take the point 1 from Figure 6 corresponding to pure water with parameters $\rho = 0.06$ g/cm^3, $T = 2.3$ kK, and $p = 600$ bar. The adiabatic expansion (with $s = \text{const}$) starting from the point 1 is a black curve shown in Figure 9.

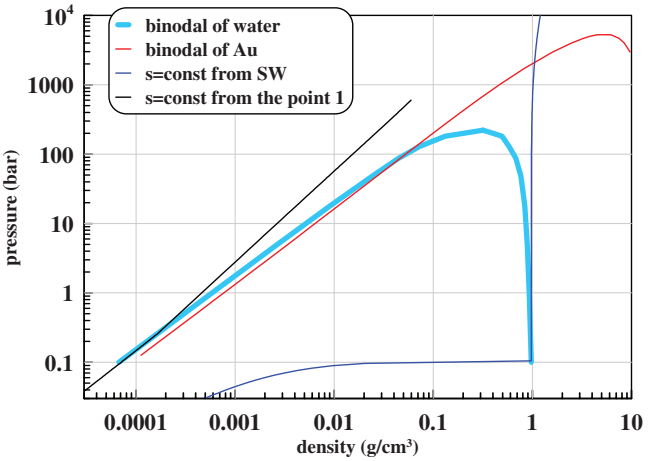

FIGURE 9 The density-pressure phase diagram is presented. The thick light blue and red curves are the phase equilibrium curves for water and gold, respectively. Two adiabatic curves for water particles are shown. One of them (the black curve) starts from the point 1 in Figure 6. The other one (the deep blue curve) begins behind a shock front compressing water to 3 GPa

We follow inflation of water along the black-coloured adiabatic curve in Figure 9 down to the expansion degree below the ambient pressure in water, which is chosen equal to 1 bar. The curve "$s=$ const from the point 1" in Figure 9 consists of the two parts corresponding to one-phase and two-phase states. Their factors $\gamma = d(\log(p))/d(\log(\rho))$ are 1.3 and 1.06, respectively. These values were similar to 1.3–1.16 given in Figure 4 in ref. [3]. The black curve intersects the binodal curve for water only at very small densities.

The adiabatic curves for gaseous water filling a bubble are concentrated near the hottest curve having maximum entropy. For a long pulse, for which a shock and dissipative heating are weak, they belong to the conductively heated layer. The adiabatic curve starting from a water particle heated by 3 GPa shock has a small degree of expansion at a final pressure of 0.1 bar. This shown as the blue curve "$s=$ const from SW" in Figure 9, where SW denotes a shock wave. Writing the mass balance between a disk of hot water and a bubble

$$\pi R_{\mathrm{L}}^2 d_{\mathrm{wt}} \rho_1 = (1/2)(4/3)\pi R_{\mathrm{bub}}^3 \rho_{\mathrm{fin}}, \tag{3}$$

one can find that the maximum radius (at which the minimum p is achieved) is $R_{\mathrm{bub}} \approx 800$ μm. This value is less than $R_{\mathrm{bub}} \approx 1.4$ mm measured in ref. [3]. In (3), we assume that $R_{\mathrm{L}} = 250$ μm as in ref. [3], $\rho_1 = 0.06$ g/cm^3 is the density in the point 1 in Figure 6, $\rho_{\mathrm{fin}} = 6 \times 10^{-5}$ g/cm^3 is the average density of two-phase water at the end point of the black curve in Figure 9. We put the thickness of a layer of hot water equal to $d_{\mathrm{wt}} = 5$ μm according to (2).

6 | CONCLUSION

The ablation of gold in water by laser pulses with different durations and absorbed energies was investigated. Estimates based on Stokes's law demonstrate that we can neglect the creep of gold NPs with diameters <10 nm relative to gaseous water surrounding them. We found that NPs are mixed with gaseous water in the hot water layer as shown in Figure 8. Thus, those NPs fill a bubble of gaseous water. Their concentration and sizes differ. The outer and inner NPs are created earlier than the NPs filling the middle range of radii inside the bubble, see Figure 8. Successive expansions and collapses of the bubble mix this spatially differentiated distributions.

REFERENCES

[1] D. Zhang, B. Gökce, S. Barcikowski, *Chem. Rev.* **2017**, *117*, 3990.
[2] J. Xiao, P. Liu, C. X. Wang, G. W. Yang, *Progr. Mater. Sci.* **2017**, *87*, 140.
[3] J. Lam, J. Lombard, C. Dujardin, G. Ledoux, S. Merabia, D. Amans, *Appl. Phys. Lett.* **2016**, *108*, 074104.
[4] N. A. Inogamov, V. V. Zhakhovskii, V. A. Khokhlov, *J. Exp. Theor. Phys.* **2018**, *127*, 79.
[5] M. E. Povarnitsyn, T. E. Itina, P. R. Levashov, K. V. Khishchenko, *Phys. Chem. Chem. Phys.* **2013**, *15*, 3108.
[6] C.-Y. Shih, C. Wu, M. V. Shugaev, L. V. Zhigilei, *J. Colloid Interface Sci.* **2017**, *489*, 3.
[7] C.-Y. Shih, R. Streubel, J. Heberle, A. Letzel, M. V. Shugaev, C. Wu, M. Schmidt, B. Gokce, S. Barcikowski, L. V. Zhigilei, *Nanoscale* **2018**, *10*, 6900.
[8] R. Fang, A. Vorobyev, C. Guo, *Light Sci. Appl.* **2017**, *6*, e16256.
[9] N. A. Inogamov, V. V. Zhakhovskii, V. A. Khokhlov, *J. Exper. Theor. Phys.* **2015**, *120*, 15.
[10] A. A. Samarskii, *The Theory of Difference Schemes*, 1st ed., CRC Press, Boca Raton, Florida, **2001**.
[11] A. V. Bushman, V. E. Fortov, G. I. Kanel, A. L. Ni, *Intense Dynamic Loading of Condensed Matter*, Taylor & Francis Translation, London **1993**.

[12] K. V. Khishchenko, S. I. Tkachenko, P. R. Levashov, I. V. Lomonosov, V. S. Vorob'ev, *Int. J. Thermophys.* **2002**, *23*, 1359.
[13] I. V. Lomonosov, *Laser Part. Beams* **2007**, *25*, 567.
[14] Tables of equations of states. http://teos.ficp.ac.ru/rusbank/ (accessed: December 2018).
[15] Tables of equations of states. http://www.ihed.ras.ru/rusbank/ (accessed: December 2018).
[16] Y. V. Petrov, N. A. Inogamov, K. P. Migdal, *JETP Lett.* **2013**, *97*, 20.
[17] Y. V. Petrov, N. A. Inogamov, S. I. Anisimov, K. P. Migdal, V. A. Khokhlov, K. V. Khishchenko, *J. Phys. Conf. Ser.* **2015**, *653*, 012087.
[18] Y. V. Petrov, K. P. Migdal, N. A. Inogamov, S. I. Anisimov, *JETP Lett.* **2016**, *104*, 431.
[19] N. A. Inogamov, V. V. Zhakhovskii, S. I. Ashitkov, V. A. Khokhlov, Y. V. Petrov, P. S. Komarov, M. B. Agranat, S. I. Anisimov, K. Nishihara, *Appl. Surf. Sci.* **2009**, *255*, 9712.
[20] V. V. Zhakhovskii, N. A. Inogamov, Y. V. Petrov, S. I. Ashitkov, K. Nishihara, *Appl. Surf. Sci.* **2009**, *255*, 9592.
[21] K. P. Migdal, N. A. Inogamov, Yu. V. Petrov, V. V. Zhakhovsky, *arXiv* **2017**, [cond-mat.mtrl-sci].
[22] Thermal properties of water. https://www.engineeringtoolbox.com (accessed: December 2018).
[23] N. Inogamov, V. Zhakhovsky, V. Khokhlov, *AIP Conf. Proc.* **2018**, *1979*, 190001.
[24] N. Inogamov, V. Zhakhovsky, V. Khokhlov, *arXiv* **2018**, 1803.07343v1.
[25] R. I. Nigmatulin, R. K. Bolotnova, *High Temp.* **2011**, *49*, 303.
[26] D. S. Ivanov, A. Blumenstein, J. Ihlemann, P. Simon, M. E. Garcia, B. Rethfeld, *Appl. Phys. A* **2017**, *123*, 744.
[27] V. A. Khokhlov, N. A. Inogamov, V. V. Zhakhovsky, Yu. V. Petrov, *arXiv* **2018**, [cond-mat.mes-hall], 1811.11990.
[28] A. Y. Vorobyev, C. Guo, *Opt. Express* **2006**, *14*, 2164.
[29] A. Y. Vorobyev, C. Guo, *Appl. Phys. Lett.* **2008**, *92*, 041914.
[30] V. V. Zhakhovskii, N. A. Inogamov, K. Nishihara, *JETP Lett.* **2008**, *87*, 423.
[31] V. Zhakhovskii, N. Inogamov, K. Nishihara, *J. Phys.: Conf. Ser.* **2008**, *112*, 042080.
[32] S. I. Ashitkov, P. S. Komarov, A. V. Ovchinnikov, E. V. Struleva, V. V. Zhakhovskii, N. A. Inogamov, M. B. Agranat, *Quantum Electron.* **2014**, *44*, 535.
[33] N. A. Inogamov, V. V. Zhakhovsky, S. I. Ashitkov, Y. N. Emirov, A. Y. Faenov, T. A. Pikuz, M. Ishino, M. Kando, N. Hasegawa, M. Nishikino, T. Kawachi, M. B. Agranat, A. V. Andriash, S. E. Kuratov, I. I. Oleynik, *J. Phys.: Conf. Ser.* **2014**, *500*, 112070.
[34] C. Wu, L. V. Zhigilei, *J. Phys. Chem. C* **2016**, *120*, 4438.
[35] A. A. Ionin, S. I. Kudryashov, S. V. Makarov, A. O. Levchenko, A. A. Rudenko, I. N. Saraeva, D. A. Zayarny, C. R. Nathala, W. Husinsky, *Laser Phys. Lett.* **2016**, *13*, 025603.
[36] A. Abou-Saleh, E. T. Karim, C. Maurice, S. Reynaud, F. Pigeon, F. Garrelie, L. V. Zhigilei, J. P. Colombier, *Appl. Phys. A* **2018**, *124*, 308.
[37] E. Stratakis, M. Barberoglou, C. Fotakis, G. Viau, C. Garcia, G. A. Shafeev, *Opt. Express* **2009**, *17*, 12650.
[38] E. V. Barmina, M. Barberoglu, V. Zorba, A. V. Simakin, E. Stratakis, K. Fotakis, G. A. Shafeev, *Quantum Electron.* **2009**, *39*, 89.
[39] S. I. Kudryashov, I. N. Saraeva, V. N. Lednev, S. M. Pershin, A. A. Rudenko, A. A. Ionin, *Appl. Phys. Lett.* **2018**, *112*, 203101.
[40] I. N. Saraeva, S. I. Kudryashov, A. A. Rudenko, M. I. Zhilnikova, D. S. Ivanov, D. A. Zayarny, A. V. Simakin, A. A. Ionin, M. E. Garcia, *Appl. Surf. Sci.* **2019**, *470*, 1018.
[41] J. Cleŕouin, P. Noiret, V. N. Korobenko, A. D. Rakhel, *Phys. Rev. B* **2008**, *78*, 224203.
[42] M. French, T. R. Mattsson, R. Redmer, *Phys. Rev. B* **2010**, *82*, 174108.

How to cite this article: Petrov Y, Inogamov N, Zhakhovsky V, Khokhlov V. Condensation of laser-produced gold plasma during expansion and cooling in a water environment. *Contributions to Plasma Physics*. 2019;e419. https://doi.org/10.1002/ctpp.201800180